J. Fluid Mech. (2008), *vol.* 597, *pp.* 233–259. © 2008 Cambridge University Press
doi:10.1017/S0022112007009810 Printed in the United Kingdom

Measured scaling properties of the transition boundaries in a rotating suspension of non-Brownian settling particles

W. R. MATSON[1], B. J. ACKERSON[1] AND P. TONG[2]

[1]Department of Physics, Oklahoma State University, Stillwater, OK 74078, USA
[2]Department of Physics, The Hong Kong University of Science and Technology, Clear Water Bay, Kowloon, Hong Kong

(Received 12 September 2005 and in revised form 10 October 2007)

Series of concentration and velocity patterns are found for the rotating suspension of non-Brownian settling particles in a completely filled horizontal cylinder. Individual flow states, or phases, are studied using both side and cross-sectional imaging to examine the detailed flow structures. The overall steady-state phase diagram of the system is mapped over a wide range of the rotation rate and fluid viscosity. Effects of the particle radius a, volume fraction ϕ, and cylinder radius R on the transition boundaries are examined. It is found that the phase diagram of the rotating suspensions can be divided into three regions, in which the transition boundaries obey different scaling laws. A theoretical attempt is made to understand the scaling behaviour of the transition boundaries. The theoretical understanding is achieved at three different levels: a general dimensional consideration, a scaling analysis on the continuum equations of motion, and a specific instability calculation for the transition boundary at the centrifugal limit.

1. Introduction

Many industrial processes in chemical, metallurgical, plastics, pharmaceutical, and food processing involve particulate two-phase flows (Roco 1996; Schaflinger 1996; Crowe, Sommerfeld & Tsujiet 1998). Because of their fundamental importance and wide applications, particulate two-phase flows have become an active research area in recent years. Uniform hard-sphere particles suspended in a Newtonian fluid, in which thermodynamic forces, Brownian forces, and inertial effects are unimportant, represent a model system for the study of particulate flows. Although the single-particle motion is known with high precision, the collective behaviour of the particles often shows interesting but unexpected features (Roco 1996; Voltz, Pesch & Rehberg 2001). The fluid in the suspension can generate long ranged hydrodynamic interactions between the particles, resulting in various interesting concentration and velocity patterns. Because of the long-ranged hydrodynamic interactions, the particle configuration and the solution rheology are strongly coupled to the flow field, making the suspension dynamics an interesting and challenging problem in statistical physics and low-Reynolds-number hydrodynamics.

Herein we consider a particulate two-phase flow system consisting of a suspension of uniform non-Brownian settling particles completely filling a horizontal rotating cylinder. The system is driven out of equilibrium by two external forces. First, because the particles chosen are heavy and relatively large (with radius $a \simeq 100\,\mu\text{m}$), they settle under gravity with a large Stokes velocity $U_0 = 2\Delta\rho g a^2/(9\eta)$, where $\Delta\rho = \rho_p - \rho_f$ is the density difference between the particle and fluid (solvent), g is the gravitational acceleration, and η is the fluid (solvent) viscosity. As a result, the Péclet number, given by $Pe = aU_0/D_0$, is between 6.5×10^8 and 1.2×10^{10}. Here $D_0 = k_B T/(6\pi\eta a)$ is the Stokes–Einstein diffusion constant for a single particle with thermal energy $k_B T$. This implies that the Brownian motion of the particles is negligible and the particle configurations are determined completely by the hydrodynamic interactions between the particles. Second, the entire system is under a uniform rotation, which gives rise to a centrifugal force, $\rho\omega^2 r$, for the suspension. Here ρ is the suspension density (which depends on the particle concentration), ω is the rotation rate of the cylinder and r is the radial position inside the cylinder. Because the cylinder is completely filled, there is no free surface affecting the dynamics of the system (Boote & Thomas 1999; Thomas *et al.* 2001; Tirumkudulu, Tripathi & Acrivos 1999; Tirumkudulu, Mileo & Acrivos 2000; Timberlake & Morris 2002; Duong, Husoi & Shinbrot 2004; Raiskinmaki *et al.* 2003).

Even for such a seemingly simple system, the dynamics is found to be very rich and complex. The rotating suspension has many experimental parameters, including the rotation rate ω, fluid viscosity η, particle radius a, volume fraction ϕ, density difference $\Delta\rho$, cylinder length L and radius R. These parameters give rise to multiple velocity and time scales for the system. Without a theory, it is difficult to know which dimensionless parameters control the system. As a result, one has a huge parameter space to explore experimentally. Several independent experiments have been carried out recently for different rotating suspensions. The experiments by Seiden *et al.* (Lipson & Seiden 2002; Seiden, Lipson & Franklin 2004; Seiden, Ungarish & Lipson 2005) studied the formation of alternating bands of high and low particle concentrations spaced along the rotation axis of the cylinder. They measured the average band spacing λ as a function of the ratio L/R. The suspension system used in the experiments consisted of millimetre-sized particles dispersed in water and other low-viscosity fluids. A complication caused by using such large particles is that the Reynolds number based on the particle size and the settling velocity, $Re_1 = 2aU_0\rho_f/\eta$, becomes very large. For example, the values of Re_1 for the polystyrene and silica spheres used in these experiments were between 6.5 and 735. In this case, the inertial effect of the individual particles becomes significant. It is known that the dynamics of inertial particles is qualitatively different from that of non-inertial particles. This is true even for the motion of a single particle (Happel & Brenner 1973; Tsao & Koch 1995).

Breu, Kruelle, & Rehberg (2003, 2004) studied the concentration patterns formed in the rotating suspension of glass beads. In one experiment (Breu *et al.* 2003), they investigated how the uniform monolayer of particles coating on the inner wall of the rotating cylinder under the influence of strong centrifugal force at high rotation rate develops an instability, when the rotation rate is reduced below a critical value. Such an instability causes the particle layer to collapse and form radially symmetric rings on the inner wall of the cylinder. This transition is similar to that between the discontinuous banding and centrifugal limit phases, to be discussed in § 3.1. The experiment by Breu *et al.* was carried out using a suspension of $300\,\mu\text{m}$ diameter glass beads in water. The particle-based Reynolds number Re_1 for this suspension is still very large ($Re_1 \simeq 20$). In another experiment Breu *et al.* (2004) found 'travelling waves' in a rotating suspension of $300\,\mu\text{m}$ diameter glass beads in an aqueous solution of glycerin. Given our results, though in a different region of parameter space, we postulate that the onset of the travelling waves reported by Breu *et al.* is associated with the transition from the fingering flow I to fingering flow II phases, to be discussed in § 3.1. Because narrow strip images (512×2 pixels) were used for flow visualization in the experiment by Breu *et al.*, only the axial (horizontal) motion of a thin horizontal layer of particles was recorded and the three-dimensional structure of the concentration and velocity fields was not studied.

While the experiments discussed above (Lipson & Seiden 2002; Seiden *et al.* 2004, 2005; Breu *et al.* 2003, 2004) revealed several interesting concentration and flow patterns in the system, they were conducted only in an isolated and rather limited parameter space. Therefore, these studies have not revealed dimensionless control parameters for the rotating suspensions. Theoretical arguments and calculations (Lipson & Seiden 2002; Seiden *et al.* 2004, 2005; Breu *et al.* 2003, 2004; Lee & Ladd 2002, 2005) have been used to explain the observed flow patterns, but they made different assumptions and predictions. A generally accepted theoretical framework for the rotating suspension is yet to be obtained. To verify the assumptions and test the theoretical predictions, it is essential to conduct careful and systematic measurements in a well-characterized suspension and study the overall steady-state phase behaviour of the system over a wide range of parameter space. Therefore, we choose a suspension system consisting of uniform glass spheres with radius $a = 100\,\mu\text{m}$ in an aqueous solution of glycerin with two mass concentrations to cover a fluid viscosity range from 8 to 100 cP. In this range of fluid viscosity, the particle-based Reynolds number Re_1 varies from 9.4×10^{-2} to 7.5×10^{-3} (Matson *et al.* 2005), suggesting that the rotating suspensions used in our experiment have a negligible particle inertia effect. The aims of the experiment are (i) to reveal the overall phase behaviour of the rotating suspensions and (ii) to study how the concentration and flow patterns as well as their transition boundaries change with the experimental control parameters mentioned above.

Recently, we reported the results of an experiment with fixed values of particle radius a, volume fraction ϕ, density difference $\Delta\rho$, cylinder radius R and length L, but with varying vales of rotation rate ω and fluid viscosity η (Matson, Ackerson & Tong 2003; Matson *et al.* 2005). The rotating cylinder used in the experiment was a Plexiglas tube with a fixed inner radius $R = 0.955\,\text{cm}$ and full length $L = 22.75\,\text{cm}$. The particles used were uniform glass spheres with radius $a = 100\,\mu\text{m}$ and density difference $\Delta\rho \simeq 1.19\,\text{g}\,\text{cm}^{-3}$. The volume fraction of the particle suspension was fixed at $\phi = 0.023$. Hereafter, we refer to this experimental system as the 'standard system.' The standard system showed a series of concentration and velocity patterns, or phases, over varying values of ω and η. The overall steady-state phase diagram of the system was carefully studied and the transition boundaries between different phases were mapped out over a wide range of the rotation rate and fluid viscosity.

In this paper, we report an experimental study of the effects of particle radius a, cylinder radius R, and volume fraction ϕ on the pattern formation in rotating suspensions. In the experiment to be presented below, we choose a new value for a ($= 52\,\mu\text{m}$) and R ($= 1.85\,\text{cm}$), which are different from those in the standard system by a factor close to two. The value of ϕ is varied between 1.1 % and 2.6 %. The overall phase behaviour of the rotating suspensions is carefully examined and the change of the transition boundaries between different phases is measured as a function of ω and η for different values of a, R, and ϕ. While accurate determination of the phase boundaries is a tedious and lengthy process, such an effort is essential for the understanding of the overall dynamics of the system and the transition mechanism between different phases. Knowing the shape of the phase boundaries and their

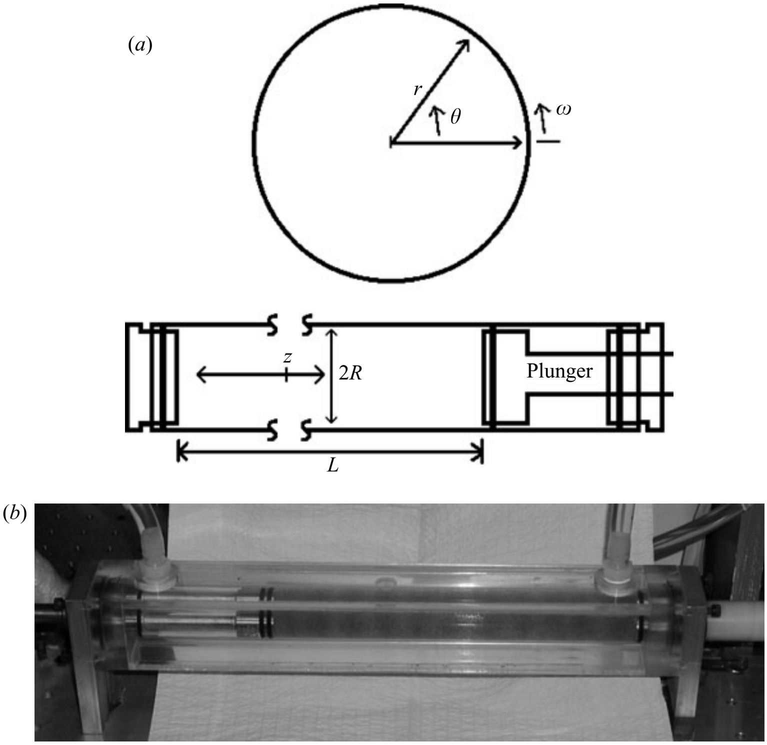

Figure 1. (*a*) Construction of the rotating cylinder and the space coordinates used in the presentation of the measurements. (*b*) The experimental setup.

dependence on the relevant experimental parameters will help us to find the scaling relations among the control parameters and to identify the dominant forces involved in each of the steady-state phases.

In addition to its fundamental importance, the study of rotating suspensions is also relevant to a wide range of practical applications. Understanding of the dynamics of rotating suspensions is required for computer modelling, process control, and various industrial applications of rotating drum mixers, including the design of rotating reactors/mixers to minimize the sedimentation effect without using microgravity (Roberts, Kornfeld & Fowlis 1991; Lipson 2001). In the following we first describe the main experimental results and provide an overall picture of how the concentration and velocity patterns formed in the rotating suspensions change with a, R, and ϕ. We then present, in the discussion section, dimensional and scaling analyses on the transition boundaries between different phases and a theoretical calculation for the transition boundary at the centrifugal limit.

2. Experiment

Figure 1 shows the construction of the rotating cylinder and the experimental setup. The rotating cylinder is a Plexiglas tube and is mounted horizontally on a thermally isolated aluminum stand. Details about the apparatus have been described in Matson *et al.* (2005), and here we mention only some key points. Two brass ends are milled to fit the tube and sealed with two o-rings. A sliding plunger is built similarly inside the tube, so that the length L of the tube to be filled with a solution can be varied.

A threaded plug is installed at the centre of the plunger to remove air from the tube. Most measurements are carried out with a full tube length $L = 22.75 \pm 0.05$ cm. The cylinder rotates freely on two ball bearings inside a square cooling chamber, which has an inch of clearance around the cylinder. The temperature of the cooling chamber is maintained constant by circulating cold (hot) water from a temperature controlled bath/circulator. The temperature stability of the circulator is 0.05°C, which provides fine control of the fluid viscosity. The cooling chamber is made of flat transparent Plexiglas plates to admit incident light and to observe the light scattered by the particles. The use of the flat window eliminates the optical distortions generated by the curvature of the cylinder sidewall and thus improve the quality of optical imaging. The base plate of the aluminum stand is equipped with adjustable legs to facilitate precision levelling of the cylinder and anchor holes to keep the entire system fixed firmly on an optical table.

Figure 1(a) also shows the space coordinates to be used below in the presentation of the measurements. The origin of the coordinate system is chosen to coincide with the centre of the rotating cylinder; r and θ are, respectively, the radial and azimuthal directions in the rotation plane and the z-axis is along the axis of symmetry (the rotation axis) of the cylinder. The cylinder is driven by a stepper motor. A thermally insulated coupler is used to prevent motor heat from entering the cylinder system. A micro-stepping drive controller regulates the motor position with a resolution of 2.5×10^4 steps/rotation. The controller is stimulated by a home-made indexer, which provides an accuracy of $2.5 \times 10^{-2} \pm 2.5 \times 10^{-5}$ s in the rotation period T. This fine control of the rotation period (or the rotation rate $\omega = 2\pi/T$) allows us to determine the boundary of each dynamic phase accurately.

The cylinder is filled completely with an aqueous solution of glycerin with a small amount of liquid detergent (0.25 vol. %) added to prevent particle aggregation. Two aqueous solutions of glycerin are used to cover a fluid viscosity range from 8 to 100 cP. One aqueous solution has 60 wt. % mass concentration of glycerin and its viscosity varies from 8 to 22 cP when the temperature of the solution is changed from 30 to 5°C. The other aqueous solution has 77 wt. % mass concentration of glycerin and its viscosity varies from 19 to 100 cP when the temperature of the solution is changed from 44°C to 6°C (Matson 2004). In the experiment, we vary the solution temperature by changing the temperature of the cooling chamber with a temperature stability of 0.05°C.

To vary the experimental control parameters, we use three sample systems in the experiment. The first system uses a rotating cylinder with inner radius $R = 0.955 \pm 0.02$ cm. The particles used are uniform glass spheres with an average density $\rho_p = 2.35\,\mathrm{g\,cm^{-3}}$. The density difference between the particles and the liquid is $\Delta\rho = \rho_p - \rho_s \simeq 1.19\,\mathrm{g\,cm^{-3}}$. The particle radius is $a = 100\,\mu\mathrm{m}$ and the size variation is less than 8 %. The volume fraction of the particle suspension is fixed at $\phi = 0.023$. We refer to this system as the 'standard system.' The second system is the same as the standard system except that smaller particles are used. The average particle radius is changed from 100 μm to 52 μm. These particles have somewhat larger size variations with a standard deviation of approximately 30 %. Hereafter, we refer to this system as the 'small-particle system'. The third system is also the same as the standard system except that the inner radius of the rotating cylinder is increased from 0.955 cm to 1.85 ± 0.02 cm. Hereafter, we refer to this system as the 'large-cylinder system'.

For the standard system with fluid viscosity rangeing from 8 to 100 cP, the corresponding Stokes velocity U_0 varies from 3.25 to $0.26\,\mathrm{mm\,s^{-1}}$. There are two length scales and two velocity scales in the problem, which give rise to four definitions of the Reynolds number. The Reynolds number based on the particle size and the settling velocity, $Re_1 = 2aU_0\rho_f/\eta$, varies from 9.4×10^{-2} to 7.5×10^{-3} in the viscosity range mentioned above. The Reynolds number based on the particle size and wall speed is given by $Re_2 = 2aR\omega\rho_f/\eta$, which ranges from 3 to 0.2 for a maximum rotation rate $\omega \simeq 4\pi\,(\mathrm{s}^{-1})$. The Reynolds number based on the cylinder radius and wall speed, $Re_3 = R^2\omega\rho_f/\eta$, ranges from 1.7×10^2 to 13 for $\omega \simeq 4\pi\,(\mathrm{s}^{-1})$. The Reynolds number based on the cylinder radius and the settling velocity is given by $Re_4 = RU_0\rho_f/\eta$, which varies from 2.9×10^{-2} to 4.5.

In the experiment, we use a standard video imaging technique to record the motion and spatial distribution of the particles. A video charge-coupled-device (CCD) camera records particle images in different cross-sectional planes of the cylinder (r, θ-plane) and in the vertical (θ,z)-plane passing through the axis of rotation of the cylinder. To facilitate the imaging in the (r,θ)-plane (end view), we construct a special short cell ($L = 2.25 \pm 0.03\,\mathrm{cm}$) with the same diameter as the longer cylinder but having a transparent end window for video imaging. The short cell rotates freely on a ball bearing inside a square cooling chamber and is connected to a drive motor outside the cooling chamber. A sheet of laser light of 1 mm in thickness is used to illuminate a (r,θ)-plane of the cell. The whole cell is mounted on a translational stage, so that the flow visualization in the (r,θ)-plane can be carried out at different locations along the z-axis. The imaging of the long cylinder in the vertical (θ,z)-plane (side view) is carried out using back-lit illumination. Particle trajectories are visible as streaks in superposed consecutive images. To vary the contrast of the particle images, we use both blue and translucent white glass spheres.

3. Experimental results

3.1. *General phase behaviour of the standard system*

The standard system exhibits a total of ten different steady states (or dynamic phases) and they are distinguished in the experiment by their unique flow patterns and particle distributions. At low rotation rates, the particles lie and slide on the bottom floor of the cylinder, forming a fluidized granular bed. At very high rotation rates, the centrifugal force becomes dominant and all the particles are spun onto the cylinder wall. Between the two extremes, we observed a series of different concentration and velocity patterns in the rotating suspension. Figure 2 shows the ‘phase diagram’ of the standard system as a function of the rotation period $2\pi/\omega$ and fluid viscosity η. It is reproduced here to provide a global comparison between the phase diagrams obtained in different rotating suspensions.

We first briefly review each of the phases in order of their appearance with increasing ω. A detailed description of the flow states in the standard system can be found in Matson *et al.* (2005). This review serves as an introduction to the small-particle and large-cylinder systems, as both of them exhibit the same number of steady states. The steady states in these two systems show similar behaviour to those in the standard system, and they differ only in their locations in the phase diagram. In this section we discuss the common features of the steady states in all three systems, and the differences between these systems will be discussed in the following sections. Figure 3 shows the side view of the particle distribution for different steady states in the standard system. These images were taken using back lighting. Regions with higher particle population absorb and scatter more light and thus appear darker. Similar particle distributions are also observed in the small particle and large cylinder systems.

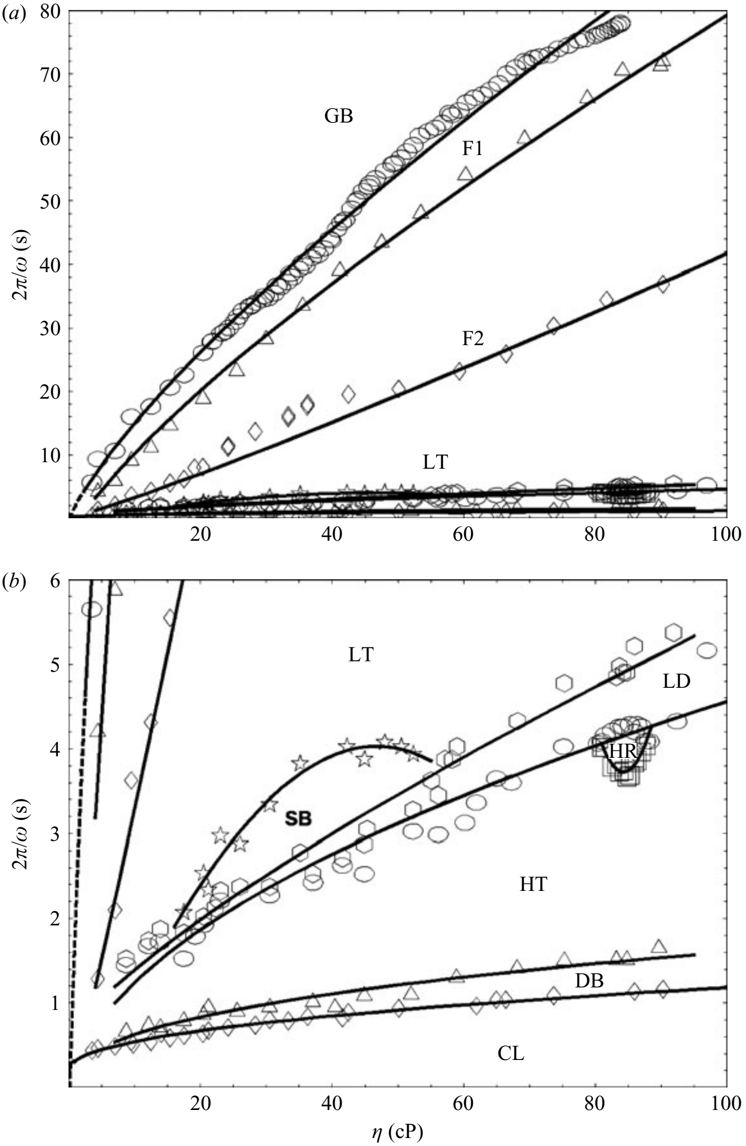

FIGURE 2. (*a*) Overall phase diagram of the standard system in the plane of the rotation period $2\pi/\omega$ and fluid viscosity η. (*b*) An enlarged part of the phase diagram for high-rotation-rate states. The symbols are experimentally determined data points and the solid lines are spline-fitted smooth curves for the phase boundaries. The dashed lines are the extrapolated curves from the fit. GB: granular bed, F1: fingering flow I, F2: fingering flow II, LT: low-rotation-rate transition, SB: stable bands, LD: local-structure drop-off, HR: homogenous region, HT: high-rotation-rate transition, DB: discontinuous banding, and CL: centrifugal limit.

Granular bed (GB) When ω is zero, the particles lie on the cylinder floor as a loosely packed granular bed. As the cylinder rotates, the bed is carried up the rising wall. Under gravity the inner layer of particles in contact with the solvent slide downward, creating a circulation within the bed. A steady state is reached, which results in a fluidized granular flow similar in appearance to that observed for a viscous liquid in a

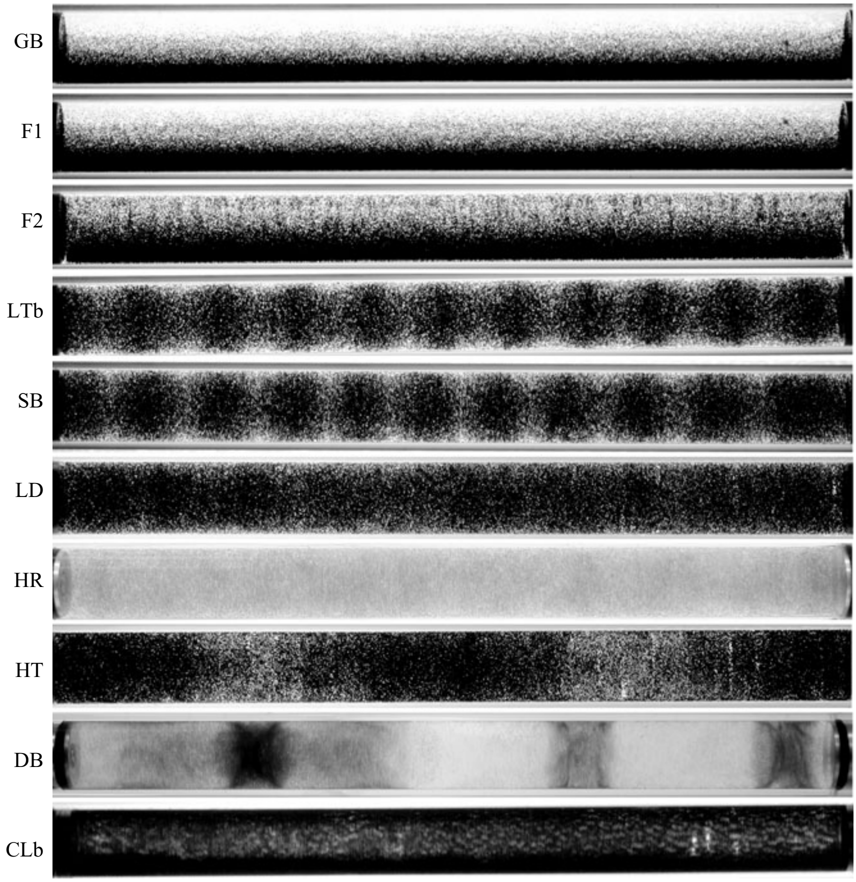

FIGURE 3. Side view of the particle distribution for different flow states in the standard system. Darker regions contain more particles. GB: granular bed, F1: fingering flow I, F2: fingering flow II, LTb: low-rotation-rate transition without a granular bed, SB: stable bands, LD: local-structure drop-off, HR: homogenous region, HT: high-rotation-rate transition, DB: discontinuous banding, and CLb: centrifugal limit with all particles on the cylinder wall.

partially filled rotating cylinder (Thoroddsen & Mahadevan 1997). This gravity-driven flow produces a counter rotation in the pure liquid in the central region of the cell. With larger ω, the top leading edge of the bed moves into the upper half of the cell and the particles are injected into and become suspended in the pure liquid region.

Fingering flow I (F1) Particles in the F1 phase behave differently from those in the GB phase on a microscopic level. In the GB phase, particles are mostly contained in the granular bed region. Those particles travelling near the upper part of the bed move downward together with the bed with the same velocity and they join the bed downstream in a relatively short period of time. In the F1 phase, however, particles leave the top, or leading edge of the bed, as a two-dimensional sheet. This is an unstable situation leading to a Rayleigh–Taylor-like instability (Chandrasekhar 1961; Youngs 1984) with particles clumping together into lines or fingers. Initially, two or three particles line up loosely in the flow and then grow into chain-like structures of several millimetres in length and a few particle diameters in width. We call this 'finger formation' and hence the resulting flow is called 'Fingering flow'. As ω increases, the fingers grow both in number and size, and so does their settling velocity relative to the rotating background. The fingers are distributed along the z-axis uniformly. When a finger falls, it follows the granular bed, keeping its radial position r nearly constant until it reaches the base of the bed.

Fingering flow II (F2) As mentioned above, the fingers become larger with increasing ω and thus produce larger disturbances to the flow field in the closed cylinder. The fingers in the F2 phase are large enough to become visible in the side view image shown in figure 3 (F2). The thin vertical dark strands on the upper half of the tube are the growing fingers, which are distributed quite uniformly along the z-axis. These thin dark strands are invisible in figure 3 (F1). Closer examination of the finger detachment near the top leading edge of the granular bed reveals that the fingers in the F1 phase detach from the rising wall at fixed locations of approximately equal distance apart along the cylinder when viewed from the side. In going from the F1 to F2 phases, we find that the detaching position of the settling fingers begins to drift over a small horizontal distance. As a result, the falling fingers when viewed at a fixed downstream location appear to have a zigzag-like trajectory as a function of time. Careful particle tracking reveals that the fingering flow is essentially two-dimensional, independent of z in both the F1 and F2 phases.

Low-rotation-rate transition (LT) The onset of the low-rotation-rate transition is marked by the development of an axial component (v_z) of the finger velocity. The motion of the fingers becomes three-dimensional when the fingers start to fall toward the centre of rotation at larger rotation rate. Further increasing ω results in the fingers falling next to the downward-moving cylinder wall. Once this occurs, the granular bed is quickly dissolved and all the particles remain suspended. The LT phase has a transition character, which is unique when compared with the other phases discussed above. Near the lower ω boundary, the system behaves more like F2. As the system moves toward the larger ω boundary, the fingering flow behaviour diminishes and the system starts to resemble the stable band phase, to be discussed below. The band-like appearance is clearly seen in figure 3 (LTb). Particles form periodic bands along the z-axis with a distinct self-reinforcing flow structure. Before reaching the transition boundary between the LT and SB phases, however, these bands are unstable and fluctuate both in time and spatial orientation in a quasi-periodic fashion.

Stable bands (SB) Once the lower ω boundary of the SB phase is reached, the fluctuating velocity components parallel to the rotation axis disappear, and the bands become stationary in space. As shown in figure 3 (SB), the bands are structurally identical and are separated alternately by void regions. The position of the bands remains fixed for a given ω with fairly uniform spacing, except near the cylinder ends. The average spacing between the bands is $\lambda = 2.2$ cm, which is 1.2 ± 0.1 times the tube diameter. Our measurements of the band spacing with different values of ω, η, R, a, and ϕ reveal that the average band spacing changes only with the cylinder radius R and is independent of the other control parameters. Lipson *et al.* (Lipson & Seiden 2002; Seiden *et al.* 2004, 2005) also reported band formation for nearly neutral buoyant particles in water and other low-viscosity fluids. While their experimental uncertainties are relatively large, the measured band spacing is comparable to our result. They also found that the average band spacing changes with the cylinder length L. However, our measurements carried out in the $L = 22.75$ cm and $L = 2.25$ cm cylinders show that the steady-state behaviour of the phase diagram for the three suspension systems remains unchanged with L.

Local-structure drop-off (LD) At even larger ω, the secondary flow pattern associated with the band structure cannot keep up with the increased cylinder rotation and the band structure decays. At first, one segment of the bands disappears and that region appears uniform at a lower particle concentration. The other band segments remain unchanged with little or no adjustment in axial location. However, they may absorb particles to increase the gravitational force required to maintain the remaining structure. This is shown in figure 3 (LD). Once the drop-off process starts at a given location, it spreads along the z-axis in both directions with increasing ω. It is found that the local-structure drop-off is a reversible process. Reducing the rotation rate reverses the process and restores all the destroyed structures to their original position.

Homogeneous region (HR) For high-viscosity solutions, the drop-off process continues with increasing ω until all the bands disappear from the entire cylinder. As shown in figure 3 (HR), the spatial distribution of the particles in the HR phase is fairly uniform throughout the cylinder. The HR phase is extremely sensitive to the levelling of the rotating cylinder and a slight tilt of less than a tenth of a degree will result in a notable concentration gradient along the tube length. In the experiment, we were able to keep the cylinder at a perfectly levelled state for several weeks to demonstrate the steady-state nature of the HR phase. It is seen from figure 2 that the HR phase occupies a small island region of the phase space, indicating that a delicate balance among the governing forces is required for this particular flow state.

High-rotation-rate transition (HT) The high-rotation-rate transition is characterized by large-scale concentration variations along the rotation axis (z-axis). As shown in figure 3 (HT), the particles migrate and form three concentrated (dark) regions extending along the z-axis. The dark regions are several centimetres in length and are separated by two less populated (light) regions. Usually we see two or three concentrated regions along the entire length of the cylinder. There is no obvious secondary flow associated with this structure, as in the case of the SB and LD phases. The exact number and the location of the concentrated regions vary with ω and η but seem to be independent of L. Similar to the situation in the LT phase, the HT phase also resembles a coexistent state. Near the lower ω boundary, the system resembles the LD phase with a background concentration variation. As the system moves toward the larger ω boundary, the concentrated regions shrink and the system behaves more like the DB phase, to be discussed below.

Discontinuous banding (DB) The DB phase shows sharp and well-separated dense regions of particles having no regular spacing. Hereafter, we refer to these dense regions of particles as segregation bands. The region between the segregation bands is free of particles. Figure 3 (DB) shows the concentration profile of the DB phase along the z-axis. When viewed from the side, the segregation bands have particles on or near the cell wall as well as a ball-shaped collection of particles near the axis of rotation. The ball of particles is diffuse and occupies more than half the space between the cell walls. At the lower frequency boundary of this phase, particles are ejected along the axis of rotation and follow an irregular trajectory bringing them back to the band at the outer wall. This observation suggests some sort of secondary flow, which is out (away) from the band along the axis of symmetry and toward the band along the cell walls. The absence of particles between these bands also suggests some secondary flow that both forms and maintains the band structure. One possible source of the secondary flow is a streaming flow produced by the motion of particles within the band structure itself. In the rotating frame with angular velocity ω, the ball of particles as a whole may oscillate under the alternating gravitational force $\rho \boldsymbol{g}$ of frequency ω. Such an oscillatory motion of particles could generate a steady streaming flow (Riley 2001; Voth *et al.* 2002) to maintain the band structure of this phase.

Centrifugal limit (CL) The large-ω limit of the phase diagram is the centrifugal limit, at which all the particles spin out to the cylinder wall under the influence of the centrifugal force. Given enough time, all patterns present on the cylinder wall are eliminated and a uniform coating layer of particles is generated on the wall. Figure 3 (CLb) shows the side view of this coating layer. The transition from the DB phase to the CL phase is one of the sharpest transitions discussed so far: it is sharper than our resolution in the rotation period, which is 25 ms per rotation, and is completely reversible. In other words, a change of less than 2.5 % in rotation period (25 ms out of 1 s at $\eta \simeq 60$ cP, see figure 2) will cause all the particles to spin out to the cylinder wall. Going back to the previous setting will recreate the segregation bands at exactly the same axial locations.

3.2. *Particle size dependence*

We first examine the response of the rotating suspension when the particle radius a is changed to $a = 52\,\mu$m. The measurements in the standard system (Matson *et al.* 2005) show that the transition boundaries in figure 2 result from a balance of the competing forces acting on the rotating suspension over varying values of ω and η. When the particle size (or cylinder radius) is changed, new balances are established. Thus a close examination of how the transition boundaries respond to the change of the key experimental parameters will provide new insight into the nature of the competing forces responsible for each transition. This will also help us to find the dimensionless control parameters of the system. Figure 4 shows the phase diagram of the small-particle system in the plane of the rotation period $2\pi/\omega$ and fluid viscosity η. It exhibits the same number of steady states as the standard system. These steady states share features with the standard system, but the location of the transition boundaries in the small-particle system moves considerably in the plane of $2\pi/\omega$ and η. In particular, the three low-rotation-rate boundaries shift significantly to smaller values of ω. To facilitate further theoretical analysis, we provide the numerical values of all the measured transition boundaries in table 2, which is available as a supplement to the online version of the paper.

It is important to note that the observed transition boundaries HT/DB and DB/CL are independent of the particle size. This finding suggests that the governing forces associated with the high-rotation-rate states can be described by a course-grained approach and a continuum theory may be possible. The HR phase is recovered in the small-particle system. The rotation rate for the onset of the HR phase is slightly smaller than that of the standard system, but the viscosity range of the HR phase remains almost unchanged. This indicates that the small-particle system requires smaller values of the rotation rate to achieve near homogeneous mixing. As mentioned above, reducing the particle size by a factor close to 2 (and hence the particle settling velocity U_0 is reduced by a factor of almost 4) generally decreases the rotation rate necessary for each transition boundary. The transition boundaries in the low-rotation-rate regime are affected most.

3.3. *Cylinder radius dependence*

We now discuss how the rotating suspension responds to the change of the cylinder radius to $R = 1.85$ cm. Figure 5 shows the phase diagram of the large-cylinder system in the plane of the rotation period $2\pi/\omega$ and fluid viscosity η. Except for the HR phase, the large-cylinder system recovers all the steady states in the standard system. These steady states share features with the standard system, but the location of the transition boundaries in the large-cylinder system shifts considerably in the plane of $2\pi/\omega$ and η. It is found that all the transition boundaries depend on the cylinder radius. Increasing

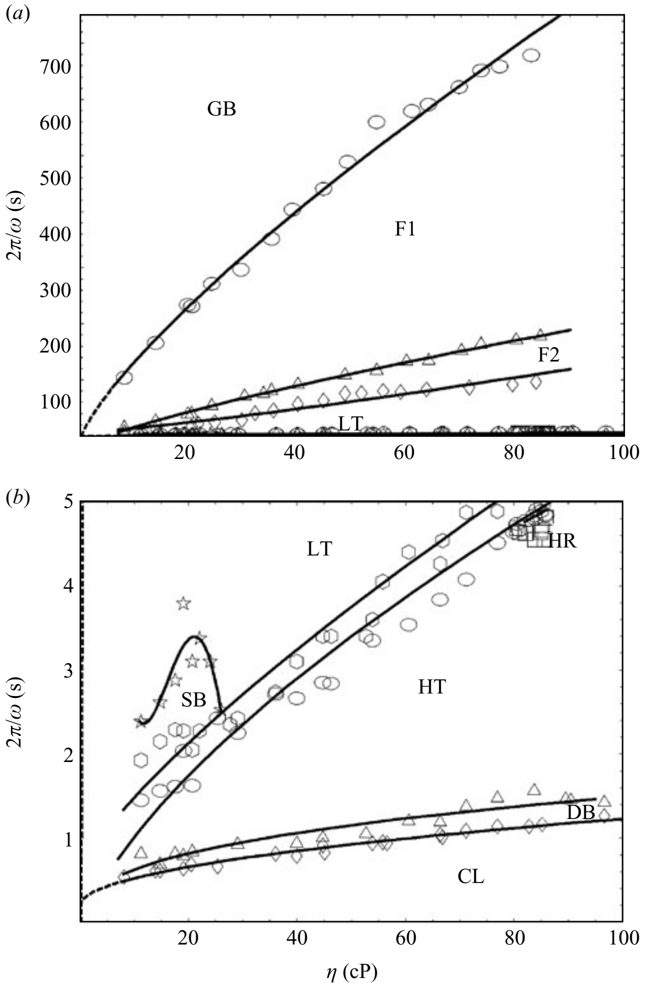

FIGURE 4. (*a*) Overall phase diagram of the small-particle system in the plane of $2\pi/\omega$ and η. (*b*) An enlarged part of the phase diagram for high-rotation-rate states. The symbols are experimentally determined data points and the solid lines are spline-fitted smooth curves for the phase boundaries. The dashed lines are the extrapolated curves from the fit. Letter symbols are the same as in figure 2.

the cylinder radius by a factor close to 2 generally decreases the rotation rate necessary for each transition boundary. The HR phase, which is located in the viscosity range of ~80 cP for the standard system, could not be reproduced in the large-cylinder system. It may move to a higher viscosity range beyond the reach of the current experiment. The numerical values of all the transition boundaries in the large cylinder system are also given in table 2 (available with the online version of the paper).

3.4. *Particle concentration dependence*

In addition to the study on how the particle size and cylinder radius affect the steady states of the rotating suspension, we also investigated the effect of the particle concentration on four high-rotation-rate boundaries: the onset boundaries of the LD and HT phases (labelled LD-onset and HT-onset, respectively, in table 1) and the HT/DB and DB/CL boundaries. In the experiment, we choose three fixed values

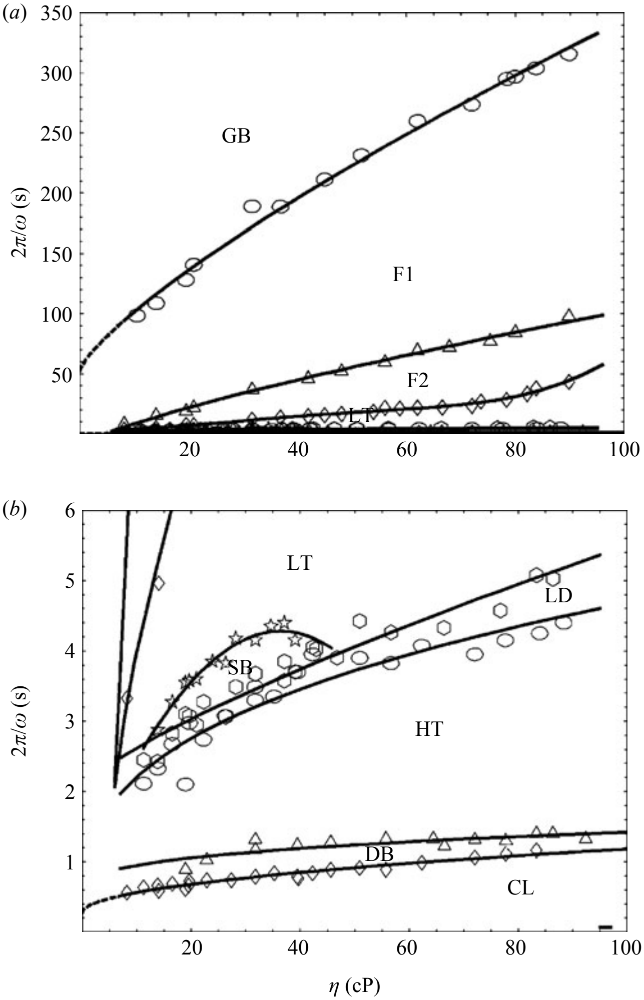

FIGURE 5. (*a*) Overall phase diagram of the large-cylinder system in the plane of $2\pi/\omega$ and η. (*b*) An enlarged part of the phase diagram for high-rotation-rate states. The symbols are experimentally determined data points and the solid lines are spline-fitted smooth curves for the phase boundaries. The dashed lines are the extrapolated curves from the fit. Letter symbols are the same as in figure 2.

of the fluid viscosity along the transition boundaries in the standard system and observe how the location of each transition boundary changes with the particle volume fraction ϕ. The numerical values of the four transition boundaries measured at different values of η are given in table 1. Figure 6 shows an example of the measured concentration dependence for the HT-onset boundary at three fixed values of η: 71.06 cP (circles), 37.29 cP (triangles), and 20.81 cP (pluses). The four transition boundaries all follow the same general trend that the rotation rate required for each transition boundary increases with increasing ϕ. This finding suggests that the dominant effect of increasing particle concentration is not an increase of the effective fluid viscosity, which would lower the rotation rate necessary for each transition boundary; rather, it is the increase of the gravitational driving force due to the increase of the total particle mass that causes the increase of ω with ϕ. The data also reveal a

η (cP)	ϕ (%)	LD-onset $2\pi/\omega$ (s)	HT-onset $2\pi/\omega$ (s)	HT/DB $2\pi/\omega$ (s)	DB/CL $2\pi/\omega$ (s)
71.06	1.06	7.35	6.65	1.34	1.26
	1.47	6.35	5.26	1.34	1.19
	1.88	5.58	4.88	1.34	1.14
	2.29	4.63	3.94	1.34	1.11
	2.70	4.78	3.45	1.34	1.11
37.29	1.06	4.10	3.45	1.34	1.04
	1.47	3.65	3.08	1.24	0.96
	1.88	3.45	2.79	1.21	0.84
	2.29	3.05	2.66	1.19	0.81
	2.70	2.66	2.41	1.09	0.74
20.81	1.06	3.13	2.93	1.14	0.66
	1.47	2.55	2.48	1.11	0.66
	1.88	2.68	2.38	1.09	0.74
	2.29	2.33	2.13	1.06	0.74
	2.70	2.23	1.95	1.04	0.64

TABLE 1. Numerical values of the measured transition boundaries as a function of ϕ in the standard system at three fixed values of fluid viscosity. Some of the transition boundaries are plotted in figure 6.

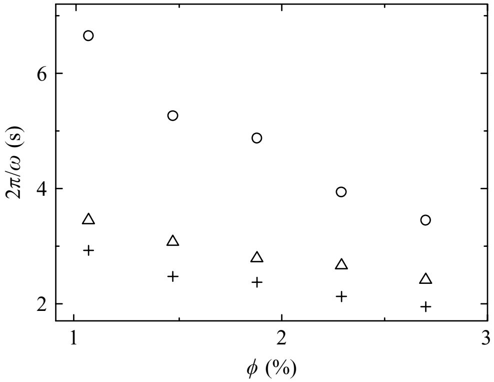

FIGURE 6. Measured concentration dependence of the onset boundary of the HT phase in the standard system at three fixed values of fluid viscosity: $\eta = 71.06$ cP (circles), 37.29 cP (triangles), and 20.81 cP (pluses).

viscosity-dependent character. As shown in figure 6, the high-viscosity portion of the transition boundary is more sensitive to the concentration changes. We also examined the transition boundaries of the HR phase in the standard system and found that they remain unchanged over the concentration range studied.

4. Discussion

The experimental results discussed above provide new insight into the scaling behaviour of the transition boundaries in the rotating suspensions. The experiment indicates that the phase diagram of the rotating suspensions can be divided into three regions. In the low-rotation-rate regime (Regime I), which includes the GB, F1, F2, and part of LT phases, hydrodynamic interactions resulting from the settling of individual particles are important. The settling of the particles is balanced by the lift of the upward moving wall, giving rise to a strong dependence of the transition boundaries on both a and R. In the high-rotation-rate regime (Regime III), which includes the HT, DB, and CL phases, the centrifugal force becomes important. The balance between the gravitational acceleration g and the centripetal acceleration $\omega^2 R$ at the cell wall gives rise to a rotation period, which has a square-root dependence on R but is independent of the particle radius a. The transition boundaries in the intermediate regime (Regime II), which includes part of LT, SB, LD, and HR phases, show a more complex behaviour, suggesting a delicate balance among the viscous, gravitational and centrifugal forces.

4.1. *Dimensional analysis of the transition boundaries*

With these observations, we now can carry out a general dimensional analysis of the transition boundaries. The first step in the dimensional analysis is to list all possible parameters for the system at hand. Here we include: N, the number of particles in the sample volume R^3; ϕ, the particle volume fraction; ρ, the suspension density; $\Delta\rho$, the density difference between the particle and fluid (solvent); ρ_f, the fluid (solvent) density; a, the particle radius; R, the cell radius; U_0, the particle sedimentation velocity; g, the acceleration due to gravity; η, the fluid (solvent) viscosity; ω, the cell rotation rate. There are three relationships connecting some of the 11 parameters listed above: $\phi = N(a/R)^3$, $U_0 = 2\Delta\rho g a^2/(9\eta)$, and $\rho = \rho_f + \Delta\rho\phi$. In addition, there are three basic units: mass, length and time. Thus we have five independent dimensionless parameters ($11 - 3 - 3 = 5$), identified as: a/R, $\eta/(\rho_f \omega R^2)$, $g/(\omega^2 R)$, $\Delta\rho/\rho_f$, and ϕ. Because $\Delta\rho/\rho_f$ is not varied in our study, we express our results in terms of the four dimensionless parameters: a/R, $1/Re_3 \equiv \eta/(\rho_f \omega R^2)$, $A \equiv \Delta\rho g/(\rho_f \omega^2 R)$, and ϕ. The volume fraction can also be viewed as a length scale ratio, $\phi \simeq (4\pi/3)(a/\ell)^3$, where ℓ is the inter-particle separation. The velocity ratio, $U_0/(\omega R)$, is not included here because it is related to A via the equation $(a/R)^{-2}[U_0/(\omega R)]/Re_3 = 2A/9$.

The transition boundaries based on a hydrodynamic theory of the suspension can be expressed as a function of the four dimensionless quantities:

$$F\left(\frac{a}{R}, \frac{1}{Re_3}, A, \phi\right) = 0. \tag{4.1}$$

As discussed in § 3.1, the fluid motion in Regime I is more closely related to the sedimentation of the particles, and thus we replace the variable A by $U_0/(\omega R)$. Furthermore, we expect the Reynolds number Re_3 to play a less important role in Regime I. In this case, (4.1) may be rewritten in the form

$$F_1\left(\frac{U_0}{\omega R}, \frac{a}{R}, \phi\right) = 0. \tag{4.2}$$

Solving for the velocity ratio $U_0/(\omega R)$, we now have

$$\frac{U_0}{\omega R} = f_1\left(\frac{a}{R}, \phi\right) \simeq f_1\left(\frac{a}{R}\right). \tag{4.3}$$

In writing the last equality of (4.3), we drop the dependence on ϕ because it is not varied in our experiment. The above analysis suggests that the transition boundaries in Regime I are determined primarily by two dimensionless parameters: $U_0/(\omega R)$ and a/R. The transition boundaries plotted in this form for the three suspension systems determine the unknown function f_1 for each boundary.

Figure 7 shows a log-log plot of three different transition boundaries in Regime I. It is seen from figure 7(*a*) that the GB/F1 boundaries obtained in three different

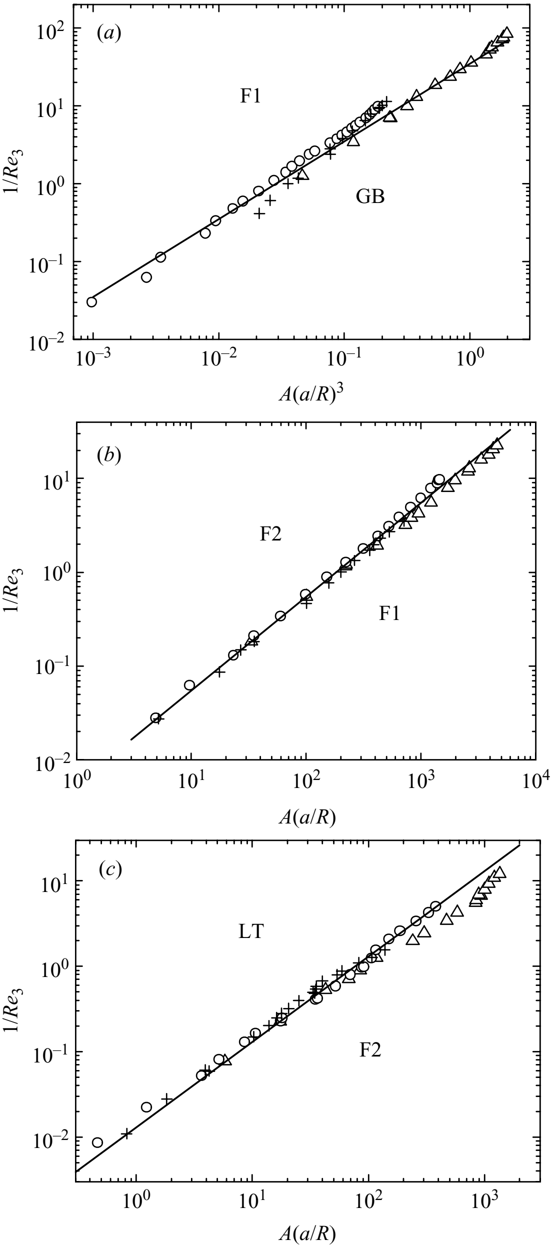

FIGURE 7. Scaling of the transition boundaries in Regime I. Circles show the standard system, triangles the small-particle system, and pluses the large-cylinder system. (*a*) Transition boundary GB/F1 in the plane of $1/Re_3$ and $A(a/R)^3$. The solid line is a power-law fit $1/Re_3 = 35A(a/R)^3$. (*b*) Transition boundary F1/F2 in the plane of $1/Re_3$ and $A(a/R)$. The solid line is a power-law fit $1/Re_3 = 5.5\times10^{-3}A(a/R)$. (*c*) Transition boundary F2/LT in the plane of $1/Re_3$ and $A(a/R)$. The solid line is a power-law fit $1/Re_3 = 1.3 \times 10^{-2}A(a/R)$.

systems collapse nicely into a single master curve when they are plotted in the plane of $1/Re_3$ and $A(a/R)^3$, which are two dimensionless variables for the experimental variables of η and ω. Curved boundaries in the linear plots shown in figures 2, 4 and 5 become a universal straight line, indicating that the GB/F1 boundary can be described by a power law, $1/Re_3 = \alpha[A(a/R)^3]^\beta$, with $\alpha = 35$ and $\beta = 1.0$ (solid line). This linear equation can be rewritten as: $U_0/(\omega R) = (2/9\alpha)(a/R)^{-1}$, which is of the form shown in (4.3). The F1/F2 boundaries obtained in the three suspension systems can also be made to coincide once they are plotted in the plane of $1/Re_3$ and $A(a/R)$. This is shown in figure 7(*b*). The F1/F2 boundary can be described by a power law, $1/Re_3 = \alpha[A(a/R)]^\beta$, with $\alpha = 5.5 \times 10^{-3}$ and $\beta = 1.0$ (solid line). Again, this linear equation can be rewritten to the form shown in (4.3): $U_0/(\omega R) = (2/9\alpha)(a/R)$. It is seen from figure 7(*c*) that the F2/LT boundaries measured in the three suspension systems also have a similar scaling form, $1/Re_3 = \alpha[A(a/R)]^\beta$, with $\alpha = 1.3 \times 10^{-2}$ and $\beta = 1.0$ (solid line). Except for a larger value of α, this equation is the same as that for the F1/F2 boundary. It should be noted that in the measurements shown in figure 7, we have varied the dimensionless parameters A and $1/Re_3$ over a wide range but the ratio a/R had just two values: 1.05×10^{-2} and 5.44×10^{-3}.

From figure 7 we find that the transition boundaries in Regime I can all be described by a simple condition: $U_0/(\omega a) = C$. The value of the constant C varies for different boundaries and also depends on a/R for the GB/F1 boundary. Recently, Lee & Ladd (2005) carried out Stokes-flow simulations for a rotating suspension in a short cylinder of aspect ratio $L/R = 0.4$. From these simulations they observed essentially all the low rotation rate phases discussed above. In addition, they identified a dimensionless rotation rate, $\omega* = \omega\ell/U_0$, as an order parameter to distinguish a new dynamic transition between a low-ω particle-segregated phase and a high-ω particle-dispersed phase where particles fill the entire volume of the rotating cylinder. Given our results, we postulate that this transition is located inside the LT phase and is at the borderline between Regimes I and II. We note that the transition condition for $\omega* = \omega\ell/U_0$ obtained from the simulations is similar to our scaling result, $U_0/(\omega a) = C$, except that the characteristic length ℓ obtained from the simulations is the inter-particle separation rather than the particle radius a. The transition boundaries shown in figure 7 are obtained at a fixed volume fraction and we have not varied the volume fraction (and hence ℓ) systematically in the experiment.

The transition boundaries in Regime III are independent of the particle size, thus we expect Re_3, A and ϕ to be the only important dimensionless parameters. In this case, (4.1) may be rewritten as

$$F_2\left(\frac{1}{Re_3}, A, \phi\right) = 0. \tag{4.4}$$

Solving for $1/Re_3$, we have

$$\frac{1}{Re_3} = f_2(A, \phi). \tag{4.5}$$

This equation suggests that the transition boundaries in Regime III are determined primarily by two dimensionless parameters: $1/Re_3$ and A (when ϕ is not varied) or a function of A and ϕ (when ϕ is varied). The transition boundaries plotted in this form for the three suspension systems determine the unknown function f_2 for each boundary.

Figure 8 shows a log-log plot of three different transition boundaries in Regime III. It is seen from figure 8(*a*) that the DB/CL boundaries obtained in three different systems collapse nicely into a single master curve when they are plotted in the plane of $1/Re_3$ and A. Curved boundaries in the linear plots shown in figures 2, 4 and 5 become a universal straight line, indicating that the DB/CL boundary can be described by a power law, $1/Re_3 \simeq \alpha A^\beta$ with $\alpha = 1.0 \times 10^{-3}$ and $\beta = 1.5$ (solid line). Similarly, the

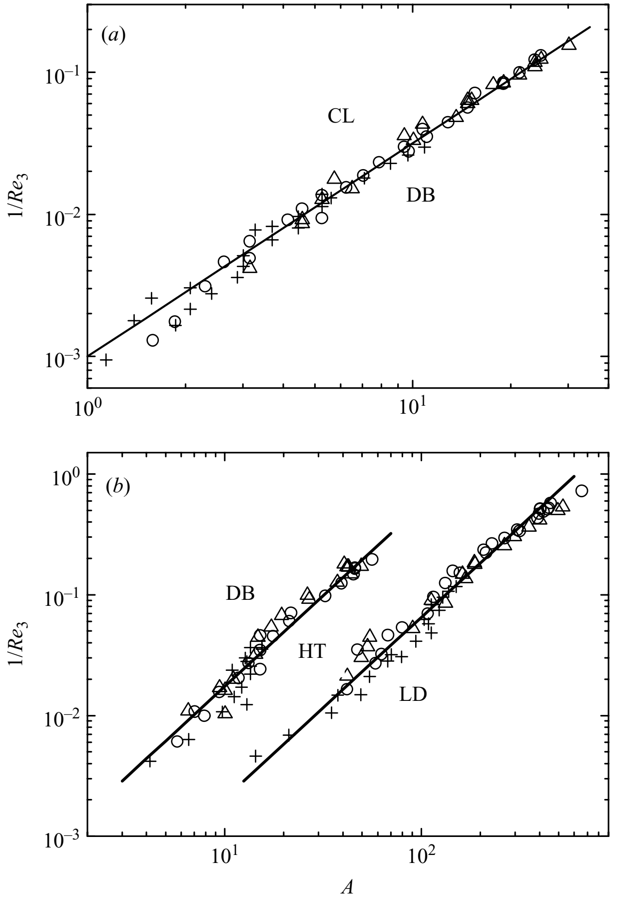

FIGURE 8. Scaling of the transition boundaries in Regime III. Circles show the standard system, triangles the small-particle system, and pluses the large-cylinder system. (*a*) Transition boundary DB/CL in the plane of $1/Re_3$ and $A = \Delta\rho g/(\rho_f \omega^2 R)$. The solid line is a power-law fit $1/Re_3 = 1.0 \times 10^{-3} A^{1.5}$. (*b*) Upper symbols: transition boundary HT/DB in the plane of $1/Re_3$ and A. The upper solid line is a power-law fit $1/Re_3 = 5.5 \times 10^{-4} A^{1.5}$. Lower symbols: transition boundary HT-onset in the plane of $1/Re_3$ and A. The lower solid line is a power-law fit $1/Re_3 = 6.5 \times 10^{-5} A^{1.5}$.

HT/DB boundaries (upper symbols in figure 8*b*) and HT-onset boundaries (lower symbols in figure 8*b*) can also be made to coincide when they are plotted in the plane of $1/Re_3$ and A. Again, both the HT/DB and HT-onset boundaries can be described by a power law, $1/Re_3 \simeq \alpha A^{\beta}$ (solid lines in figure 8*b*). The value of the exponent β $(=1.5)$ for the two boundaries is found to be the same as that obtained from figure 8(*a*). The fitted value of α varies from 5.5×10^{-4} (for the HT/DB boundary) to 6.5×10^{-5} (for the HT-onset boundary).

Figure 9 shows a log-log plot of the two remaining transition boundaries in Regime II. The transition boundary for the HR phase is not plotted here because the range of the experimental variables for this boundary is too small to have a meaningful log-log plot. Similar to the boundaries shown in figure 8, the LD-onset boundaries (shown in figure 9*a*) and LT/SB boundaries (shown in figure 9*b*) obtained in the three systems superpose nicely onto a single master curve when they are plotted in

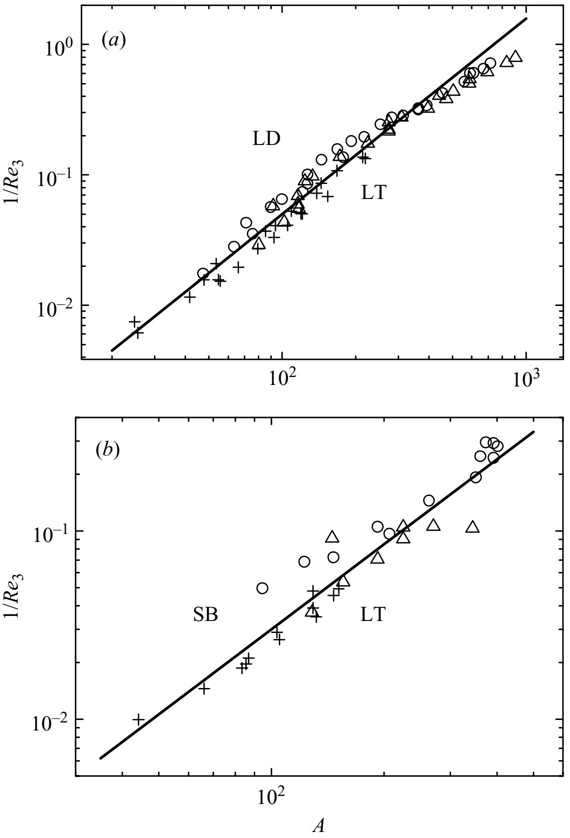

FIGURE 9. Scaling of the transition boundaries in Regime II. Circles show the standard system, triangles the small-particle system, and pluses the large-cylinder system. (*a*) Transition boundary LD-onset in the plane of $1/Re_3$ and $A = \Delta\rho g/(\rho_f \omega^2 R)$. The solid line is a power-law fit $1/Re_3 = 5.0 \times 10^{-5} A^{1.5}$. (*b*) Transition boundary LT/SB in the plane of $1/Re_3$ and A. The solid line is a power-law fit $1/Re_3 = 3.0 \times 10^{-5} A^{1.5}$.

the plane of $1/Re_3$ and A. The two boundaries can be described by a common power law, $1/Re_3 \simeq \alpha A^\beta$ (solid lines), with the same exponent $\beta = 1.5$ as those obtained in figure 8. The fitted value of α varies from 5.0×10^{-5} (for the LD-onset boundary) to 3.0×10^{-5} (for the LT/SB boundary). We notice that the high-A portion of the data ($A > 150$) in figure 9(*a*) show some deviations from the fitted power law. In a linear plot, we find that this portion of the data can also be described by a linear function $1/Re_3 \simeq \alpha' A$ (i.e. $\beta = 1.0$). In the fitting shown in figure 9(*a*) we take $\beta = 1.5$, in line with the fitting results for the other transition boundaries in Regime II.

Figures 8 and 9 thus demonstrate that the transition boundaries in Regimes II and III can all be described by a common power law, $1/Re_3 \simeq \alpha A^\beta$, with the same exponent $\beta = 1.5$. The amplitude α decreases in order of the appearance of the boundaries with increasing $2\pi/\omega$. An important implication of the power law result, $1/Re_3 \simeq \alpha A^\beta$, is that when the rotation period $2\pi/\omega$ (and hence A) goes to zero, the corresponding fluid viscosity η (and hence $1/Re_3$) also goes to zero or vice versa. From the phase diagrams shown in figures 2, 4 and 5 we find that all the transition boundaries in Regimes II and III have a finite intercept on the axis of $2\pi/\omega$ at the limit $\eta \to 0$. By equating the gravitational acceleration g with the centripetal acceleration $\omega_0^2 R$ at

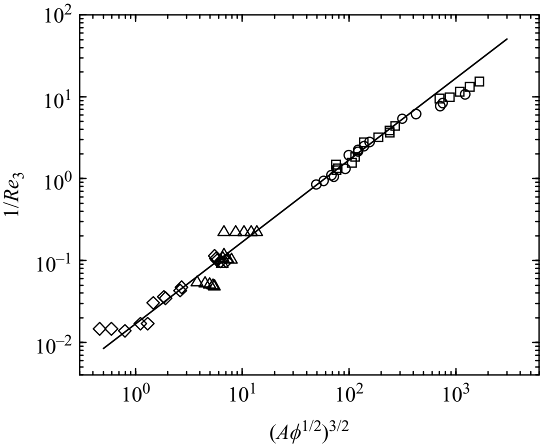

FIGURE 10. Scaling of the transition boundaries in the standard system with the volume fraction ϕ. The onset boundaries of the LD (squares) and HT (circles) phases and the HT/DB (triangles) and DB/CL (diamonds) boundaries, which are measured at different values of ϕ, are plotted in the plane of $1/Re_3$ and $(A\phi^{1/2})^{3/2}$. The solid line shows the function $1/Re_3 = 1.69 \times 10^{-2}(A\phi^{1/2})^{3/2}$.

the cell wall, we obtain a characteristic rotation period $T_0 \equiv 2\pi/\omega_0 = 2\pi\sqrt{R/g}$, which equals $(T_0)_s = 0.196$ s for the standard and small-particle systems and $(T_0)_l = 0.272$ s for the large-cylinder system. The value of T_0 is independent of η and approximates the DB/CL boundary at the low-η limit. The characteristic rotation period T_0 is the lower bound for the phase diagrams shown in figures 2, 4 and 5, below which the centrifugal force becomes so dominant that all the particles are spun onto the cell wall.

To obtain power-law fits, we define an effective rotation period $T' \equiv 2\pi/\omega' = 2\pi/\omega - 2\pi/\omega_0$, which is used in all the plots shown in figures 8 and 9. A single value of $(T_0)_s = 0.196$ s is used for all the transition boundaries in the standard and small-particle systems, suggesting that $(T_0)_s$ can be treated as a common limiting value as $\eta \to 0$ for all the boundaries in the standard and small-particle systems. In the large-cylinder system, we find the expected value of $(T_0)_l = 0.272$ s only for the DB/CL boundary. For the other transition boundaries, a slightly larger value of T_0 is needed. For example, we used $T_0 = 1.2(T_0)_l$ for the HT/DB boundary and $T_0 = 4(T_0)_l$ for all the other boundaries shown in figures 8 and 9. It is seen from figure 5 that the transition boundaries between the LT and HT phases in the large-cylinder system seem to have a larger value of the intercept and more careful measurements at the small-η limit are need to further confirm this conjecture.

We also explore the possibility of including the volume fraction ϕ into the scaling. Figure 10 shows the scaling of the transition boundaries in the standard system with the volume fraction ϕ. The onset boundaries of the LD (squares) and HT (circles) phases and the HT/DB (triangles) and DB/CL (diamonds) boundaries, which are measured at different values of ϕ (see table 1), are plotted in the plane of $1/Re_3$ and $(A\phi^{1/2})^{3/2}$. As demonstrated by figures 8 and 9, these four boundaries, when measured at a fixed value of ϕ $(= 0.023)$, can all be described by a common power law, $1/Re_3 = \alpha A^{3/2}$, with the value of α varying among the four boundaries. Once the difference in α is rescaled, the four transition boundaries will collapse into a master curve, which is represented by the solid line in figure 10 with

$\alpha = 1.0 \times 10^{-3}/\phi^{3/4} = 1.69 \times 10^{-2}$ (1.0×10^{-3} is the slope of the solid line shown in figure 8*a*). While each transition boundary shown in figure 10 is measured only in a narrow range of ϕ from 1.1 % to 2.6 %, plotting the four boundaries measured at different values of η together enlarges the dynamic range of the scaling variables. This allows us to test the scaling with the volume fraction ϕ more stringently.

The rescaling factors used for different transition boundaries are determined from the fittings shown figures 8 and 9 and no other adjustable parameter is used in figure 10. Figure 10 clearly shows that the ϕ-scaling for the four transition boundaries in Regimes II and III has a common form, $1/Re_3 = \alpha[A\phi^{1/2}]^{3/2}$, with $\alpha = 1.69 \times 10^{-2}$ (solid line). In a recent numerical simulation, Lee & Ladd (2005) showed that because of long-ranged hydrodynamic interactions between the settling particles, the inter-particle separation ℓ plays an important role in determining the dynamics of the particle-dispersed steady states (in Regimes II and III). Our finding that the four transition boundaries in Regimes II and III scale as $A\phi^{1/2} \sim A(a/\ell)^{3/2}$ suggests that these steady states have a non-trivial dependence on ℓ. It is also seen from figure 10 that the measured onset boundary of the LD phase (squares) shows some deviations from the solid line at large values of $(A\phi^{1/2})^{3/2}$. Similar deviations are also observed in figure 9(*a*).

It should be noted that figures 7–10 are obtained after many trials of plotting the data in different ways. The log-log plots in figures 7–10 are chosen to show the simple power laws discussed above. We recognize that these power laws are empirical and the data could be plotted in different ways, given that the volume fraction ϕ is varied only in a narrow range and the ratio a/R has just two values. To accommodate this, we provide the numerical values of all the measured transition boundaries in table 1 and the online suppliement table 2. In the appendix we show that the scaling results obtained above based on the dimensional analysis can also be obtained using the equations of motion for the continuous fluid (suspension) phase.

4.2. *Rayleigh–Taylor instability at the centrifugal limit*

As discussed in § 3.1, the transition between the CL and DB phases is the sharpest one observed in the rotating suspension. There is no hysteresis associated with this transition and the measured DB/CL boundary shows a viscosity dependence but is independent of the particle size (see figures 2, 4, and 5). When reducing ω toward the DB/CL boundary, the uniform coating layer of particles develops an instability, which causes it to collapse and a collection of particles falls under the influence of gravity to the centre of the cylinder and remains suspended (see figure 3 (CLa) in Matson *et al.* (2005)). This is similar to the Rayleigh–Taylor instability (Chandrasekhar 1961; Youngs 1984), where an absolutely unstable configuration of a dense fluid layer over a less dense fluid layer evolves via the fastest unstable mode of wavelength ξ_m. Given the rotation geometry shown in figure 1, one expects the coating layer of particles on the cell wall to be stable against gravity when $\omega^2 R \geqslant g$ (Sharpe 1984). Therefore, the characteristic rotation period, $T_0 = 2\pi\sqrt{R/g}$, becomes the lower bound for the DB/CL boundary, because the fluid viscosity tends to reduce the growth rate of the unstable modes (Sharpe 1984).

With the fluid viscosity included, the growth rate corresponding to the most unstable mode of wavelength ξ_m is given by (Chandrasekhar 1961; Youngs 1984)

$$\sigma_m = \sqrt{\frac{\pi g \varrho}{\xi_m}} = \frac{(g\varrho)^{2/3}}{2\nu^{1/3}}, \tag{4.6}$$

where $\varrho=(\rho_1-\rho_2)/(\rho_1+\rho_2)$ is the effective density difference between the two fluid layers and $\nu=(\eta_1+\eta_2)/(\rho_1+\rho_2)$ is their mean kinematic viscosity. For a monolayer of particles coating the inner wall of the rotating cylinder, the density is well-defined by $\rho_1 \simeq \rho_f+\Delta\rho\phi_0 R/(4a)$, where $\phi_0 R/(4a) \simeq 0.055$ is the effective volume fraction for the monolayer. The viscosity of this quasi-two-dimensional system, however, is not well-defined (Saffman 1976). Given the fact that the effective volume fraction of particles in the monolayer is not very large, we take $\eta_1 \simeq \eta_2=\eta$ for simplicity. Therefore, we have $\varrho \simeq \Delta\rho\phi_0 R/(8a\rho_f) \simeq 0.028$ and $\nu \simeq \eta/\rho_f$.

Suppose the instability requires a certain amplitude of growth in one rotation period T (faster rotations would not allow enough time for the instability to develop), then we have $T=K/\sigma_m$, where K is a proportionality constant of the order of unity. The horizontal rotation of the cylinder introduces an effective acceleration, $g-\omega^2R$, to the top portion of the particle coating layer, which then becomes the most unstable region on the cell wall. Substituting this effective acceleration into (4.6), we have

$$T[1-(T_0/T)^2]^{2/3}=T_1, \tag{4.7}$$

where $T_1=2K\nu^{1/3}/(\varrho g)^{2/3}$. Note that $T=T_0$ is the solution of T when the fluid viscosity is zero, at which $T_1=0$. Finally, substituting $T \simeq T_0+\delta$ into (4.7) and solving for δ, we obtain

$$T-T_0 \simeq \frac{T_1^{3/2}T_0^{-1/2}}{2+(3/2)(T_1/T_0)^{3/2}} \simeq \frac{K^{3/2}\nu^{1/2}}{\pi^{1/2}R^{1/4}\varrho g^{3/4}}. \tag{4.8}$$

In obtaining the last equality of (4.8), we only kept the leading-order term.

Equation (4.8) clearly shows how the two time sales T_0 and T_1 act together to determine the DB/CL boundary. To the leading order, the calculated $T-T_0$ scales with all the dimensional variables as $\nu^{1/2}/(R^{1/4}g^{3/4})$, which is in excellent agreement with the scaling result, $1/Re_3 \simeq 1.0\times10^{-3}A^{1.5}$, shown in figure 8. Using the obtained power law amplitude, we find the proportionality constant $K \simeq 4.5$, which is of the order of unity as expected. Equation (4.8) demonstrates that the modified Rayleigh–Taylor instability, for a horizontal rotating cylinder, captures the essential physics of the transition boundary between the DB and CL phases. The calculation explains both the power-law exponent and amplitude obtained from the experiment. It also provides a physical reason why an effective rotation period $T' \equiv T-T_0$ is needed for the scaling plots shown in figures 8 and 9. The simple continuum calculation, however, does not include the effect of the particle volume fraction, which presumably can be obtained only through the coupled equations for the particle phase.

5. Summary

Series of concentration and velocity patterns are found for a rotating suspension of non-Brownian settling particles in a completely filled horizontal cylinder. Individual flow states, or phases, are studied using both side and cross-sectional imaging to examine the detailed flow structures. The overall steady-state phase diagram of the rotating suspension is carefully studied and the transition boundaries between different phases are mapped out over a wide range of the rotation rate and fluid (solvent) viscosity. In the experiment, two different values of the particle radius a and the cylinder radius R are used, and the particle volume fraction ϕ varied is from 1.1 % to 2.6 %. Effects of a, R and ϕ on the pattern-forming dynamics of the system are examined carefully. It is found that the rotating suspensions with different values of a,

R and ϕ exhibit the same number of steady states. These steady states are robust and share common features among the three suspension systems studied. The location of the transition boundaries for the three systems, however, varies considerably in the plane of the rotation period $2\pi/\omega$ and fluid viscosity η.

The measured effects of a, R and ϕ provide new insight into the nature of the transition boundaries in the rotating suspension. The experiment clearly indicates that the phase diagram of the rotating suspension can be divided into three regions. In the low-rotation-rate regime (Regime I), which includes the granular bed, fingering flow I, fingering flow II, and part of the low-rotation-rate transition phases, hydrodynamic interactions resulting from the settling of individual particles are important. The settling of the particles is balanced by the lift of the upward moving wall, giving rise to a strong dependence of the transition boundaries on a, R and η. It is found that the transition boundaries in Regime I can all be described by a simple scaling relation: $U_0/(\omega a) = C$, where U_0 is the settling velocity of the particles, and the constant C varies for different transition boundaries and may also depend on the length ratio a/R.

In the high-rotation-rate regime (Regime III), which includes the high-rotation-rate transition, discontinuous banding, and centrifugal limit phases, the centrifugal force becomes important. The balance between the gravitational acceleration g and the centripetal acceleration $\omega^2 R$ at the cell wall gives rise to a rotation period, $T_0 \equiv 2\pi/\omega_0 = 2\pi\sqrt{R/g}$, which has a square-root dependence on R but is independent of the particle radius a. The transition boundaries in the intermediate regime (Regime II), which includes part of low-rotation-rate transition, stable bands, local-structure drop-off, and homogeneous region phases, seem to require a more delicate balance among the viscous, gravitational and centrifugal forces. It is found that the transition boundaries in Regimes II and III can all be described by a common power law, $1/Re_3 = \alpha(A\phi^{1/2})^{\beta}$, where $1/Re_3 = \eta/(\rho_f \omega R^2)$ is the ratio of the viscous force to the centrifugal force and $A = \Delta\rho g/(\rho_f \omega^2 R)$ is the ratio of the buoyancy force to the centrifugal force. Curved boundaries in the linear plot become straight lines when they are plotted on log-log scales for the two scaling variables. The fitted power-law exponent is found to have the same value $\beta = 1.5$ for all the boundaries and the amplitude α decreases in order of the appearance of the boundaries with increasing $2\pi/\omega$.

In addition to the experimental investigation, a theoretical attempt is made to understand the scaling behaviour of the transition boundaries observed in the rotating suspension. A dimensional analysis is carried out for the rotating suspension. It is found that the dynamics in Regimes II and III are determined by three dimensionless parameters: A, $1/Re_3$, and the density ratio $\Delta\rho/\rho_f$. Because $\Delta\rho/\rho_f$ is not varied in the experiment, the scaling of the transition boundaries is observed only in the plane of $1/Re_3$ and A. In addition to the general scaling analysis, we also carry out a specific instability calculation for the transition boundary at the centrifugal limit. This calculation is based on a simple model for the modified Rayleigh–Taylor instability under the influence of a horizontal rotation. The calculated transition boundary as a function of η and R fits the measurements well. The calculation therefore quantitatively explains the power-law behaviour of the measured transition boundary at the centrifugal limit. It also provides a physical reason why an effective rotation period is needed for the scaling plot of the transition boundaries.

We thank Anthony J. C. Ladd for useful discussions. This work was supported in part by the National Science Foundation under Grant No. DMR-0071323. P. T. was also supported in part by the Research Grants Council of Hong Kong SAR under Grant No. HKUST-CA05/06.SC01. B. J. A. thanks the HKUST Physics Department for support of his stay in Hong Kong.

Appendix: Scaling analysis of the continuum equations of motion

To further understand the physical meaning of the observed scaling laws shown in figures 7–10, we carry out a scaling analysis on the equations of motion for the continuous fluid (suspension) phase, which are closely related to the motion of the rotating suspension in Regimes II and III. Our analysis is based on the two-fluid model (Nott & Brady 1994; Ungarish 1993) for suspensions. The macroscopic equations of motion for the rotating suspension are taken to be the conservation equations of mass and momentum. In the rotating frame with angular velocity $\boldsymbol{\omega}$, at which the entire rotating cylinder is at rest, the equations of motion for the suspension with variable density $\rho(\boldsymbol{r}, t)$, pressure $P(\boldsymbol{r}, t)$, and velocity $\boldsymbol{U}(\boldsymbol{r}, t)$ take the following form (Seiden *et al.* 2004; Tritton 1988)

$$\partial_t \rho + \nabla \cdot (\rho \boldsymbol{U}) = 0, \tag{A 1}$$

$$\rho \partial_t \boldsymbol{U} + \rho \boldsymbol{U} \cdot \nabla \boldsymbol{U} = -\nabla P + \eta \nabla^2 \boldsymbol{U} + \rho \boldsymbol{g} - \boldsymbol{\omega} \times (\boldsymbol{\omega} \times \rho \boldsymbol{r}) - 2(\boldsymbol{\omega} \times \rho \boldsymbol{U}), \tag{A 2}$$

where $\boldsymbol{g}$ is the gravitational acceleration. The last two terms on the right-hand side of (A 2) are, respectively, the centrifugal and Coriolis forces. The density of the suspension is related to the volume fraction of the particles via $\rho = \rho_f + \Delta\rho\phi$, which may be solved using two additional equations similar to (A 1) and (A 2) for the particle phase (Nott & Brady 1994; Ungarish 1993).

To further simplify the equations, one needs to compare the relative weight of each of the force terms as well as the nonlinear terms in (A 2). Because there are five such terms in (A 2), there are 10 ratios (dimensionless numbers) between different terms to compare. Some are standard dimensionless numbers, such as Grashof (or Rayleigh) number, Prandtl number, Rossby number, and Ekman number, which appear in the convection and rotation problems separately (Tritton 1988). The other ratios are special ones, which appear only in this combined rotation and buoyancy-driven flow. There is no consensus in the literature about which forces dominate in each of the phases. Various theoretical models have been proposed with emphasis on different forcing terms and no serious attempt is made to compare the relative weight among the relevant forces involved in the problem. Part of the difficulty comes from the fact that the relative weight of the forcing terms changes with the rotation rate and so does the phase behaviour of the system. The measured phase diagrams shown in figures 2, 4, and 5 provide accurate numerical values, allowing us to give a concrete estimate of the relative weight among the relevant forces involved.

The velocity $\boldsymbol{U}$ in (A 2) is the relative velocity with respect to the uniform rotation. By observing the motion of the particles over a period of time, we find that the rotation rate of the suspension in Regime II is approximately the same as that of the cylinder. However, because of variations of the particle concentration, the rotation centre of the particle trajectories is shifted by an amount of ΔR relative to the rotation axis of the cylinder. Figure 11 shows a cross-sectional view of particle trajectories in the SB phase. It is seen that the particle trajectories in the (r, θ)-plane is exclusively clockwise but the 'centre' of the particle trajectories does not coincide with the axis of rotation. The relative velocity U in this case is just the secondary flow associated with the bands and scales as $U \simeq \omega \Delta R$. For a single (heavy) particle in a uniform rotating

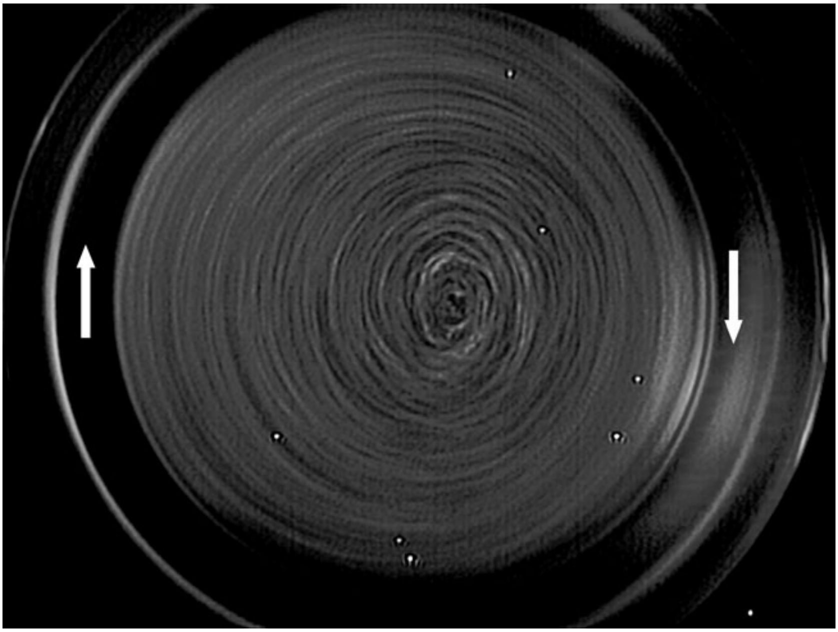

FIGURE 11. Cross-sectional view of particle trajectories in the SB phase, taken in the less populated band region with the smallest particle concentration. For clarity, 30 sequential images taken at time intervals of 1/10 s are superimposed. The arrows indicate the direction of the cylinder rotation. There are a few small defect spots on the optical window, which appear as stationary bright spots in the picture when the intensity of the illuminating light sheet is low. A solid-state laser of wavelength 532 nm is used to generate the illuminating light sheet.

fluid, this relation holds exactly (Seiden *et al.* 2005; Roberts *et al.* 1991). The ratio of this relative velocity to the linear velocity of the cell wall is thus $U/(\omega R) \simeq \Delta R/R$. From figure 11 we find that a typical value of $\Delta R/R$ is $\Delta R/R \simeq 0.16$. In fact, this is probably the largest value of $\Delta R/R$ in Regime II. As the system moves toward the large-ω end of Regime II (i.e. in the LD phase), the secondary flow associated with the stable bands cannot keep up with the increased cylinder rotation and the band structure decays, with ΔR being reduced gradually toward zero.

In Regime III, the centrifugal force becomes more important. This is shown by the creation of a concentration gradient in the radial direction. Unlike the structures in Regime II, which show large concentration variations only along the cylinder length (the z-axis) but not in the (r, θ)-plane (see figure 11), the structures in Regime III are azimuthally symmetric (no apparent θ dependence) but show significant variations of the particle concentration in the radial direction (r-dependence). This concentration gradient can produce an additional pressure gradient (Nott & Brady 1994), balancing the centrifugal force in the positive radial direction. The relative velocity U in Regime III is found to be small compared with that in Regime II. The concentration patterns in Regime III appear to rotate almost rigidly with the cylinder.

With these observations, we can now estimate the relative weight of various terms in (A 2). We first carry out our analysis in Regime II. From figure 2 we choose a typical point in the SB phase with $\omega \simeq 2\,\mathrm{s}^{-1}$ and $\nu \simeq \eta/\rho_f \simeq 0.35\,\mathrm{cm}^2\,\mathrm{s}^{-1}$. The centrifugal force $\boldsymbol{\omega} \times (\boldsymbol{\omega} \times \rho \boldsymbol{r})$ scales as $\rho\omega^2 R$. The Reynolds number Re_r, which is a ratio of the nonlinear terms to the viscous force, is given by $Re_r = \rho \boldsymbol{U} \cdot \nabla \boldsymbol{U}/(\eta \nabla^2 \boldsymbol{U}) \simeq UR/\nu \simeq 0.8$. The Rossby number Ro, which is a ratio of the nonlinear terms to the Coriolis force, is given by $Ro = \rho \boldsymbol{U} \cdot \nabla \boldsymbol{U}/(2\boldsymbol{\omega} \times \rho \boldsymbol{U}) \simeq U/(2\omega R) \simeq 0.08$. Therefore, the nonlinear terms in (A 2) can be ignored. The ratio of the Coriolis force to the gravitational force is given by $2(\boldsymbol{\omega} \times \rho \boldsymbol{U})/(\rho \boldsymbol{g}) \simeq (2\Delta R/R)(\omega^2 R/g) \simeq 1.2 \times 10^{-3}$, suggesting that the Coriolis force is less important than the gravitational force. Finally, we compare the centrifugal force with the gravitational force. The ratio of the centrifugal force to the gravitational force is given by $(\boldsymbol{\omega} \times (\boldsymbol{\omega} \times \rho \boldsymbol{r})/(\rho \boldsymbol{g}) \simeq \omega^2 R/g \simeq 3.9 \times 10^{-3}$, suggesting that in Regime II the centrifugal force is less important than the gravitational force. In Regime III, however, the centrifugal force needs to be included. The nonlinear terms and the Coriolis force remain small in Regime III, because they are associated with a smaller value of U.

With the above numerical estimations, (A 1) and (A 2) can be simplified into the following form in Regimes II and III:

$$\partial_t \rho + \nabla \cdot (\rho \boldsymbol{U}) = 0, \tag{A 3}$$

$$\rho \partial_t \boldsymbol{U} \simeq -\nabla P + \eta \nabla^2 \boldsymbol{U} + \delta\rho \boldsymbol{g} + \boldsymbol{\omega} \times (\boldsymbol{\omega} \times \delta\rho \boldsymbol{r}), \tag{A 4}$$

where $\delta\rho = \rho - \rho_f$ and the two constant force terms, $\rho_f \boldsymbol{g}$ and $\boldsymbol{\omega} \times (\boldsymbol{\omega} \times \rho_f \boldsymbol{r})$, have been absorbed into the pressure gradient term (Tritton 1988). By non-dimensionalizing (A 3) and (A 4) with respect to the length R, the velocity $R\omega$, the liquid density ρ_f, and the density difference $\Delta\rho$, we have

$$\rho \partial_t \boldsymbol{U} - A[\delta\rho \hat{\boldsymbol{y}} - \nabla P] - \frac{1}{Re_3} \nabla^2 \boldsymbol{U} - \frac{\Delta\rho}{\rho_f} \boldsymbol{\omega} \times (\boldsymbol{\omega} \times \delta\rho \boldsymbol{r}) \simeq 0, \tag{A 5}$$

$$\partial_t \rho + \nabla \cdot (\rho \boldsymbol{U}) = 0, \tag{A 6}$$

where $\hat{\boldsymbol{y}}$ is a unit vector pointing to the direction of $\boldsymbol{g}$. In the above, all the flow variables (ρ, $\delta\rho$, $\boldsymbol{U}$, $\boldsymbol{\omega}$, P) and the coordinates ($\boldsymbol{r}$, t) are dimensionless, and the pressure P is scaled by $\Delta\rho g R$. The time-derivative terms are kept because the motion of the suspension in the rotating frame is under the influence of an alternating gravitational force $\rho \boldsymbol{g}$ of frequency ω.

Equation (A 5) states that the dynamics of the rotating suspension in Regimes II and III is determined primarily by three forces: viscous, buoyancy and centrifugal. Consequently, the two equations of motion are non-dimensionalized by three control parameters: $\Delta\rho/\rho_f$, A, and $1/Re_3$. As mentioned above, because the density ratio $\Delta\rho/\rho_f$ is not varied in the experiment, there are only two dimensionless parameters, A and Re_3, in our study. This conclusion is fully supported by the experimental results shown in figures 8 and 9. By comparing (A 4) and (A 5), one finds that $1/Re_3$ is actually the ratio of the viscous force to the centrifugal force, even though it has the same expression as the Ekman number, which indicates the ratio of the viscous force to Coriolis force. The parameter A represents the ratio of the buoyancy force to the centrifugal force.

From the measured phase diagrams shown in figures 2, 4, and 5, we find that while the overall viscosity dependence of the transition boundaries becomes weaker as $1/Re_3$ decreases, considerable viscosity dependence still remains in the DB/CL boundary, which has the smallest value of $1/Re_3$ among all the transition boundaries. The phase boundary measurements thus suggest that the viscous term $(1/Re_3)\nabla^2 \boldsymbol{U}$ in (A 5) cannot be ignored for our system even at the small-$1/Re_3$ limit. This is because the effect of the boundary layer close to the cylinder wall is important for our system of finite cylinder radius. While the theoretical discussion presented here proves instructive, it is nevertheless incomplete. As mentioned above, there are two additional equations of motion for the particle phase, including the conservation equation of particles which is not discussed here. A further theoretical analysis is needed in order to understand the effect of the volume fraction ϕ on the pattern formation in the rotating suspensions.

REFERENCES

Boote, O. A. M. & Thomas, P. J. 1999 *Phys. Fluids* **11**, 2020.

Breu, A. P. J., Kruelle, C. A. & Rehberg, I. 2003 *Europhys. Lett.* **62**, 491.

Breu, A. P. J., Kruelle, C. A. & Rehberg, I. 2004 *Eur. Phys. J.* E **13**, 189.

Chandrasekhar, S. 1961 *Hydrodynamic and Hydromagnetic Stability*, Chapter X. Dover.

Crowe, C., Sommerfeld, M. & Tsujiet, Y. 1998 *Multiphase Flows with Droplets and Particles.* CRC, Boca Raton.

Duong, N. P., Husoi, A. E. & Shinbrot, T. 2004 *Phys. Rev. Lett.* **92**, 224502.

Happel, J. & Brenner, H. 1973 *Low Reynolds Number Hydrodynamics*, 2nd edn. Kluwer.

Lee, J. &. Ladd, J. C. 2002 *Phys. Rev. Lett.* **89**, 104301.

Lee, J. &. Ladd, J. C. 2005 *Phys. Rev. Lett.* **95**, 048001.

Lipson, S. G. 2001 *J. Phys.: Condens. Matter* **13**, 5001.

Lipson, S. G. & Seiden, G. 2002 *Physica* A **314**, 272.

Matson, W. R. 2004 Doctoral thesis, Oklahoma State University, 2004 (available at http://physics.ust.hk/penger/Matson.pdf).

Matson, W. R., Ackerson, B. J. & Tong, P. 2003 *Phys. Rev.* E **67**, 050301(R).

Matson, W. R., Kalyankar, M., Ackerson, B. J. & Tong, P. 2005 *Phys. Rev.* E **71**, 031401.

Nott, P. R. & Brady, J. F. 1994 *J. Fluid Mech.* **275**, 157.

Raiskinmaki, P., Astrom, J. A., Kataja, M., Latva-Kokko, M., Koponen, A., Jasberg, A., Shakib-Manesh, A. & Timonen, J. 2003 *Phys. Rev.* E **68**, 061403.

Riley, N. 2001 *Annu. Rev. Fluid Mech.* **33**, 43.

Roberts, G. O., Kornfeld, D. M. & Fowlis, W. W. 1991 *J. Fluid Mech.* **229**, 555.

Roco, M. C. 1996 *Particulate Two-Phase Flow.* Butterworth-Heinemann.

Saffman, P. G. 1976 *J. Fluid Mech.* **73**, 593.

Schaflinger, U. 1996 *Flow of Particles in Suspensions.* Springer.

Seiden, G., Lipson, S. G. & Franklin, J. 2004 *Phys. Rev.* E **69**, 015301(R).

Seiden, G., Ungarish, M. & Lipson, S. G. 2005 *Phys. Rev.* E **72**, 021407.

Sharp, D. H. 1984 *Physica* D **12**, 3.

Thomas, P. J., Riddell, G. D., Kooner, S. & King, G. P. 2001 *Phys. Fluids* **13**, 2720.

Thoroddsen, S. T. & Mahadevan, L. 1997 *Exps. Fluids* **23**, 1.

Timberlake, B. D. & Morris, J. F. 2002 *Phys. Fluids* **14**, 1580.

Tirumkudulu, M., Mileo, A. & Acrivos, A. 2000 *Phys. Fluids* **12**, 1615.

Tirumkudulu, M., Tripathi, A. & Acrivos, A. 1999 *Phys. Fluids* **11**, 507.

Tritton, D. J. 1988 *Physical Fluid Mechanics*, 2nd edn., p. 215. Claredon.

Tsao, H. K. & Koch, D. L. 1995 *J. Fluid Mech.* **296**, 211.

Ungarish, M. 1993 *Hydrodynamics of Suspensions.* Springer.

Voltz, C., Pesch, W. & Rehberg, I. 2001 *Phys. Rev.* E **65**, 011404.

Voth, G. A., Bigger, B., Buckley, M. R., Losert, W., Brenner, M. P., Stone, H. A. & Gollub, J. P. 2002 *Phys. Rev. Lett.* **88**, 234301

Youngs, D. L. 1984 *Physica* D **12**, 32.